Vietnam Journal of Science and Technology ***63*** *(4) (2025) 780-791*

doi:10.15625/2525-2518/19447

Effective elemination of 4-nitrophenol in water by reduced graphene oxide/$CoFe_2O_4$/Fe nanocomposite

Vu Dinh Thao[1], Nguyen Dinh Sinh[1], Nguyen Trung Dung[1], Vu Ngoc Toan[2], Nguyen Nhat Huy[3, 4, *]

[1]*Faculty of Physical and Chemical Engineering, Le Quy Don Technical University, 236 Hoang Quoc Viet, Nghia Do Ward, Ha Noi, Viet Nam*

[2]*Insitute of New Technology, 17 Hoang Sam, Nghia Do Ward, Ha Noi, Viet Nam*

[3]*Faculty of Environment and Natural Resources, Ho Chi Minh City University of Technology (HCMUT), 268 Ly Thuong Kiet Street, Dien Hong Ward, Ho Chi Minh City, Viet Nam*

[4]*Vietnam National University Ho Chi Minh City, Linh Xuan Ward, Ho Chi Minh City, Viet Nam*

[*]Email: *nnhuy@hcmut.edu.vn*

Received: 19 November 2023; Accepted for publication: 27 June 2025

Abstract. Visible-light photocatalysts with magnetic and Fenton-like properties hold great potential for practical applications. In this study, a reduced graphene oxide/cobalt ferrite/zero valent iron (rGO/$CoFe_2O_4$/Fe) ternary material was synthesized by combining co-precipitation, hydrothermal, and reduction with $NaBH_4$, resulting in a unique nanocomposite that combines the high surface area and conductivity of rGO with the magnetic and catalytic properties of $CoFe_2O_4$ and Fe^0. The as-prepared rGO/$CoFe_2O_4$/Fe nanocomposite was characterized by FTIR, XRD, UV-Vis DRS, VSM, SEM, EDX, Raman, and BET analyses. As a result, rGO sheets were effectively covered with a high density of $CoFe_2O_4$ and Fe^0 (40 – 100 nm) nanoparticles. The rGO/$CoFe_2O_4$/Fe exhibited outstanding properties such as high saturated magnetization (31.18 emu/g at 11 kOe) with superparamagnetic property, high 4-nitrophenol (4-NP) degradation efficiency (98.78 %), fast removal rate (k = 0.0361 min^{-1}), and narrow band gap energy (1.327 eV). As an excellent magnetic visible-light photo-Fenton-like catalyst, rGO/$CoFe_2O_4$/Fe has potential wastewater treatment.

Keywords: Reduced graphene oxide, Cobalt ferrite, Zero-valent iron, Photocatalysis, 4-nitrophenol.

Classification numbers: 3.1.2., 3.7.3.

1. INTRODUCTION

4-Nitrophenol (4-NP) is quite commonly found in industrial wastewater with around 10 million tons of this type of wastewater must be treated each year [1]. Due to the benzene ring's strong structure and conjugation with the p-nitro and hydroxyl groups, 4-NP is extremely hazardous even at low concentrations in water and difficult to remove [2]. Because 4-NP can cause serious harm to biological and human health [3], the effective removal of 4-NP is essential. Among the treatment methods, the advanced oxidation processes (AOPs) is considered one of the most effective ones for removing persistent organic substances in water, especially AOPs based on sulfate radical ($SO_4^{\bullet-}$). The most common method to produce $SO_4^{\bullet-}$ is through

peroxymonosulfate (HSO_5^-, PMS) activation [4]. Compared to hydroxyl radical ($HO^•$) ($t_{1/2}$ = 10^{-3} μs, E^0 = 1.8 - 2.7 V), the $SO_4^{•-}$ has a longer half-life ($t_{1/2}$ = 30 – 40 μs) and higher standard redox potential (E^0 = 2.5 - 3.1 V). It has a more selective oxidation ability for pollutants with aromatic rings and unsaturated bonds with a higher reaction rate of 10^6 – 10^9 $M^{-1}{\cdot}s^{-1}$ in a wider pH range [5]. $SO_4^{•-}$ can be produced by the activation of peroxymonosulfate (PMS) by various agents such as light, temperature, sonication, and heterogeneous catalysts. Among them, heterogeneous catalysts are widely used due to their high efficiency, non-toxicity, low energy consumption, and low cost [6].

Heterogeneous catalysts based on nanoparticles (NPs) such as Fe and Co are widely developed to degrade organic pollutants because of their high efficiency and environmental friendliness. Among them, zero-valent iron (Fe^0) NPs can be used as a supplementary source of Fe^{2+} for Fenton-like reactions [7]. Furthermore, it can react directly with PMS to generate $SO_4^{•-}$ [8]. Recently, MFe_2O_4 magnetic NPs, especially cobalt ferrite ($CoFe_2O_4$) with special physico-mechanical properties [9] and narrow bandgap [10] have been used to activate PMS under visible light radiation [11]. With the excellent properties of Fe^0 and $CoFe_2O_4$, the $CoFe_2O_4$/Fe composite could be a promising visible-light photo-Fenton-like magnetic catalyst for the effective degradation of 4-nitrophenol in water.

Despite these advantages, $CoFe_2O_4$ and Fe^0 nanoparticles still tend to accumulate, which can lead to reduced catalyst activity [12]. Therefore, support materials such as MWCNTs, titanates, graphene, and reduced graphene oxide (rGO) [13-15] have been recently proposed. Among them, rGO could be an ideal carrier thanks to its flexibility, high mechanical strength, high chemical stability, and large surface area [16]. Furthermore, the intrinsically localized π–π electrons and the high electrical conductivity of rGO give excellent charge separation. Thus, in addition to enhancing the transit of photogenerated electrons, the combination of photocatalyst and rGO also lowers the recombination rate of charge carriers [17]. Therefore, the dispersion of $CoFe_2O_4$ and Fe^0 NPs onto rGO was proposed to enhance the catalytic activity of the composite.

In this study, rGO/$CoFe_2O_4$/Fe nanocomposite was synthesized by co-precipitation and hydrothermal methods followed by reduction. The obtained material would have a high specific surface area with the flexibility of rGO, highly efficient visible-light photocatalysis, magnetic behavior of the $CoFe_2O_4$, and Fenton-like properties of Fe^0. The characteristics of the obtained materials were comprehensively studied. The activity and application of the rGO/$CoFe_2O_4$/Fe were evaluated via its removal of 4-NP in water. The effects of environmental conditions on 4-NP degradation such as catalyst dosage, PMS concentration, and pH were studied in detail.

2. MATERIALS AND METHODS

2.1. Synthesis and characterization of rGO/$CoFe_2O_4$/Fe composite

The chemicals used were graphite flakes (AMT Co. Ltd) and sodium borohydride ($NaBH_4$, Chengdu Jinshan). Other chemicals such as ethanol, NH_4OH, NaOH, H_2SO_4, $K_2S_2O_8$, $KMnO_4$, H_2O_2, $Fe(NO_3)_3{\cdot}9H_2O$, $Fe(NO_3)_2{\cdot}6H_2O$, and $Co(NO_3)_2{\cdot}6H_2O$ were from Xilong. Deionized water was used throughout the material synthesis and catalytic test.

GO nanosheets were synthesized by a modified Hummer method [18]. Then, $CoFe_2O_4$ NPs were deposited on the prepared GO nanosheets through a co-precipitation reaction (at room temperature for 4 h) between Co^{2+}, $Fe^{3+,}$ and OH^- ions (pH = 11, by using concentrated NH_3 solution) using precursors of GO (0.03 g), $Co(NO_3)_2$ (2 mmol), and $Fe(NO_3)_3$ (4 mmol) in 200 ml DI water and stirred for 1 h before hydrothermal treatment at 150 °C for 10 h.

rGO/$CoFe_2O_4$/Fe nanocomposites were synthesized by using $NaBH_4$ to reduce and deposite Fe NPs onto rGO/$CoFe_2O_4$ surface. In a typical synthesis, a dispersion containing as-synthesized rGO/$CoFe_2O_4$ was added with 4 mmol of $Fe(NO_3)_2$. Then, 0.06 g of $NaBH_4$ was added to the solution and the reduction reaction was conducted for 2 h at ambient condition. The entire synthesis process is carried out in an N_2 environment to prevent oxidation. The as-synthesized rGO/$CoFe_2O_4$/Fe was separated using a magnet and rinsed several times with deionized water and ethanol before being dried in a vacuum oven for 12 h.

The composites were analyzed by characterizations such as X-ray diffraction (XRD, Bruker D8 Advance), Fourier-transform infrared spectroscopy (FTIR, PerkinElmer Spectrum Two), scanning electron microscopy (SEM) and energy-dispersive X-ray spectroscopy (EDX, Hitachi S-4800), Raman spectroscopy (Horiba Jobin-Yvon LabRam HR800), ultraviolet-visible diffuse reflectance spectroscopy (UV-Vis DRS, Jasco V670), and magnetization measurement using vibrating sample magnetometer (VSM, home-made system).

2.2. Photocatalytic removal of 4-NP

The removal of 4-NP in water using rGO/$CoFe_2O_4$/Fe nanocomposite as a photocatalyst was conducted under visible light irradiation at room temperature. A 40W L4X LED (highest intensity at 446 nm) was employed as the light source. In all experiments, a distance of 10 cm was maintained between the lamp and the reactor's solution. Initially, a reactor containing 100 mL of 10 mg/L 4-NP at pH 7 was added with 0.015 g of rGO/$CoFe_2O_4$/Fe and continuously aerated and stirred to achieve adsorption-desorption equilibrium in the dark for 30 min. Then, the mixture was added with 0.015 g PMS and the light was turned on to perform the photocatalytic reaction. After each 15-minute interval, water samples (4.00 mL) were taken, centrifuged, and submitted for analyzing the 4-NP concentration at 320 nm using a spectrophotometer (Biochrom Libra S60). The pH of the solution was controlled by adding 0.01 M NaOH or H_2SO_4 solutions.

The 4-NP removal efficiency (H, %) and rate constant (k, min^{-1}) are calculated as follows.

$$H = (1 - C_t/C_o)\times 100\ \% = (1 - A_t/A_o)\times 100\ \% \quad (1)$$

$$\ln(C_t/C_0) = - k\times t \quad (2)$$

where C_o and C_t are the concentration of 4-NP at the initial and t (min) time, respectively. A_o and A_t are the absorbance of 4-NP at the initial and t time, respectively.

3. RESULTS AND DISCUSSION

3.1. Characteristics of materials

The FTIR spectra of GO, rGO/$CoFe_2O_4$, and rGO/$CoFe_2O_4$/Fe composites are shown in Figure 1. In the GO spectrum (Figure 1(a)), the band at 3000 - 3500 cm^{-1} indicates O─H stretching of surface O─H and absorbed water in the graphene interlayer. The peaks at 1726, 1630, 1401, 1194, and 1030 cm^{-1} are from the vibration of carbonyl/carboxyl C═O stretching, aromatic C═C stretching, carboxyl C═O stretching, C═C stretching, and alkoxy/epoxy C─O stretching, respectively [33]. In rGO/$CoFe_2O_4$ (Figure 1(b)) and rGO/$CoFe_2O_4$/Fe (Figure 1(c)), the band of O─H stretch is very broad for GO but becomes narrower for rGO/$CoFe_2O_4$ and rGO/$CoFe_2O_4$/Fe, indicating a significant decrease in the density of OH^- groups after the reduction process. The peak at 545 cm^{-1} for rGO/$CoFe_2O_4$ and rGO/$CoFe_2O_4$/Fe are attributed to the Fe─O vibrations in $CoFe_2O_4$ [19]. Compared with GO, the characteristic peaks of the

oxygen-containing functional groups are significantly reduced or even disappeared, proving that GO has been successfully reduced to rGO.

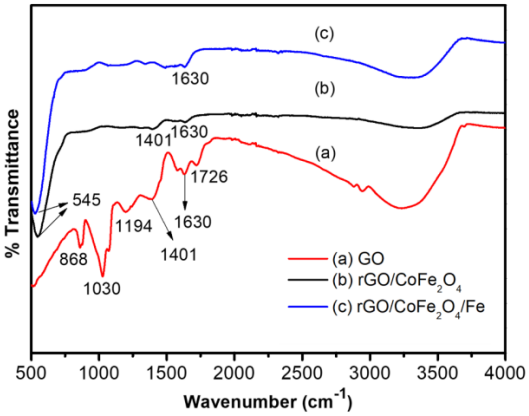

Figure 1. FT-IR spectra of (a) GO, (b) rGO/$CoFe_2O_4$, and (c) rGO/$CoFe_2O_4$/Fe.

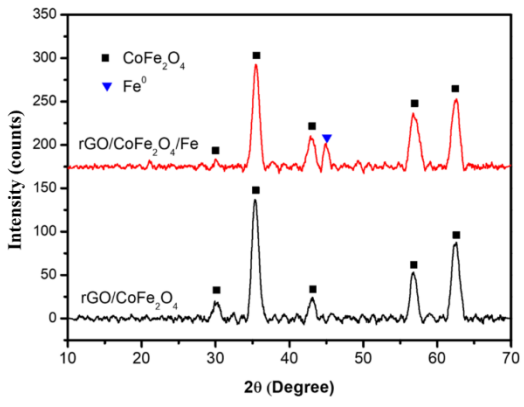

Figure 2. XRD pattern of rGO/$CoFe_2O_4$ and rGO/$CoFe_2O_4$/Fe.

The XRD pattern of rGO/$CoFe_2O_4$ and rGO/$CoFe_2O_4$/Fe are demonstrated in Figure 2. Due to the weak crystallinity of rGO, its characteristic diffraction peaks were not observed and possibly inhibited by those from $CoFe_2O_4$ and $CoFe_2O_4$/Fe NPs with dominant mass. The peaks appearing at 30.1°, 35.5°, 43.2°, 57.0°, and 62.5° are indexed to (220), (311), (400), (511), and (440) lattice planes, respectively, of spinel $CoFe_2O_4$ (JCPDS No. 22-1086) [20], indicating the crystalline nature of $CoFe_2O_4$ NPs on rGO substrate. The peaks appear at $2\theta = 44.78^o$ correspond to the (110) crystal plane of Fe^0 (JCPDS No. 06-0696) [21].

Figure 3 displays the Raman spectra of GO and rGO/$CoFe_2O_4$/Fe. Two distinct bands may be seen in the spectra of GO (Figure 3(a)), located at 1342 and 1605 cm^{-1}, corresponding to the D and G bands, respectively [22]. The D band results from the symmetry breaking of sp^2 carbon rings, which is caused by the Hummer process' oxidation of graphite and the hydrothermal reduction of GO. The G band corresponds to the vibrations scattering of photons in the sp^2 carbon plane and the prolonged vibration of the C-C bond. The Raman spectrum of rGO/$CoFe_2O_4$/Fe (Figure 3(b)) also shows D and G bands but with weaker intensity than that of GO. Specifically, in the pattern of the rGO/$CoFe_2O_4$/Fe sample, the G peak was downshifted from 1605 to 1592 cm^{-1}, due to the self-healing properties of rGO that restores the hexagonal structure of carbon atoms with defects. This result validates the successful reduction of GO to rGO. Additionally, the strength ratio between the D-band and G-band (D/G) is the basis for determining the degree of defect and the size of the sp^2 plane. This high ratio indicates that the degree of defect is large and the dimension of the sp^2 plane is reduced. The calculated I_D/I_G ratio of rGO/$CoFe_2O_4$/Fe nanocomposites was 1.117, which is higher than those of GO (1.047), indicating that GO was likewise reduced after hydrothermal treatment.

Figure 4(a) displays the SEM image where GO sheets exhibit a wrinkled and crumpled structure. The lateral side diameters of GO range from 5 to 20 μm. SEM image of rGO/$CoFe_2O_4$ nanocomposites (Figure 4(b)) depicts that on the surface of GO sheets, spherical $CoFe_2O_4$ particles with an average diameter of 50 nm are evenly dispersed. Figures 4(c-d) observe that $CoFe_2O_4$ and Fe^0 particles (with a diameter ranging from 40 to 100 nm) with high density cover the whole surface of the rGO sheets. The small diameter of the particles embedded into the

lamella of rGO is due to the large specific surface area and fast transfer of electrons, which is a major concern for visible-light photocatalysts.

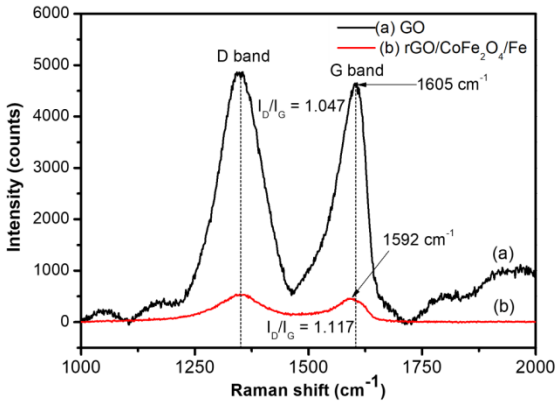

Figure 3. Raman spectra of (a) GO and (b) rGO/$CoFe_2O_4$/Fe.

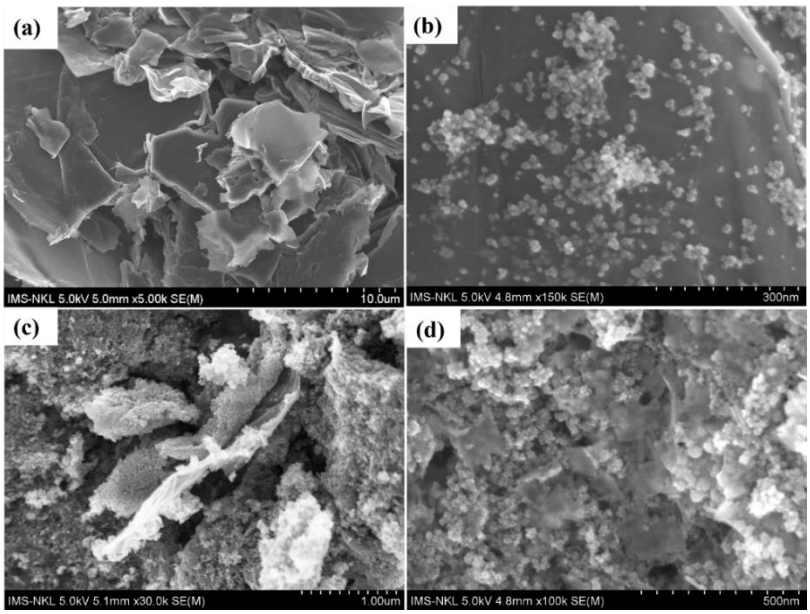

Figure 4. SEM images of (a) GO, (b) rGO/$CoFe_2O_4$, and (c-d) rGO/$CoFe_2O_4$/Fe nanocomposites at different resolutions.

The elemental composition of rGO/$CoFe_2O_4$/Fe was analyzed using EDX. The spectrum of rGO/$CoFe_2O_4$/Fe in Figure 5(a) demonstrates the detection of all components (C, O, Co, and Fe). Inset of Figure 5(a) presents the analysis results in the sample with the elemental weight percentages of 6.84 % (C), 33.32 % (O), 12.55 % (Co), and 47.29 % (Fe).

In theoretical pure rGO/$CoFe_2O_4$/Fe, there are 26.64 % of rGO and 72.46 % of $CoFe_2O_4$ and Fe^0. The GO:$CoFe_2O_4$:Fe mass ratio described in Section 1 is approximately 1.34:2.00:1.00 with theoretical mass percentages of 30.18 % (GO) and 69.40 % ($CoFe_2O_4$ and Fe^0). Because of the lowered mass percentage of oxygen caused by the reduction of GO to rGO, it was discovered that the mass percentage of rGO in the resulting rGO/$CoFe_2O_4$/Fe is lower than that of GO.

From the results of EDX analysis, it can be concluded that the material synthesis method is very effective in controlling the composition and the product obtained is of high purity.

Figure 5(b) shows that at room temperature, the rGO/$CoFe_2O_4$/Fe nanocomposite exhibits superparamagnetic behavior with the saturation magnetization (Ms) of 31.18 emu/g at 11 kOe. As a result, with an external magnetic field, the rGO/$CoFe_2O_4$/Fe nanocomposite is easily separated from the water suspension. This property of rGO/$CoFe_2O_4$/Fe nanocomposite promises many applications in heterogeneous catalysis and environmental treatment.

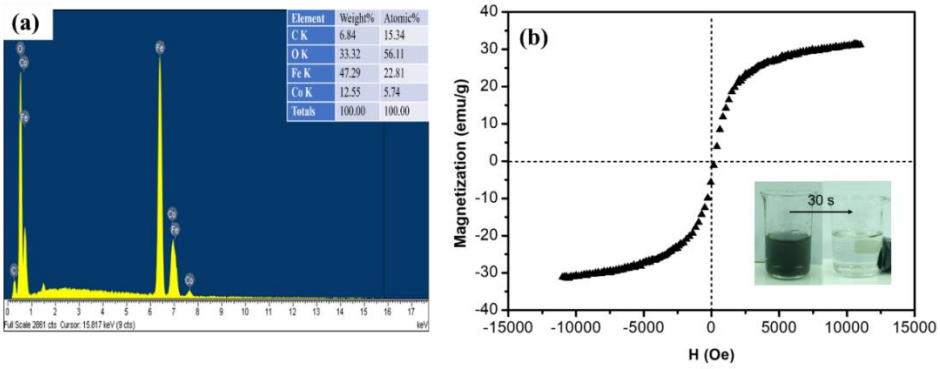

Figure 5. (a) EDX spectrum of rGO/$CoFe_2O_4$/Fe, (b) magnetization curve of rGO/$CoFe_2O_4$/Fe nanocomposite (Inset: rGO/$CoFe_2O_4$/Fe suspension before and after using a magnet for 30 s).

The porous characteristics of rGO/$CoFe_2O_4$/Fe were analyzed by N_2 adsorption–desorption isotherms, as shown in Figure 6. The isotherms display the typical type IV curves and type H3 hysteresis loop according to IUPAC classification, demonstrating the presence of mesopores in the sample. The specific surface area of rGO/$CoFe_2O_4$/Fe was calculated to be 112.68 m^2/g using the Brunauer–Emmett–Teller method (BET). The inset in Figure 6 is the pore size distribution of rGO/$CoFe_2O_4$/Fe. Based on the Barrett–Joiner–Halenda (BJH) method, a broad distribution of mesopores with an average pore size of 16.18 nm and total pore volume of 0.059 cm^3/g.

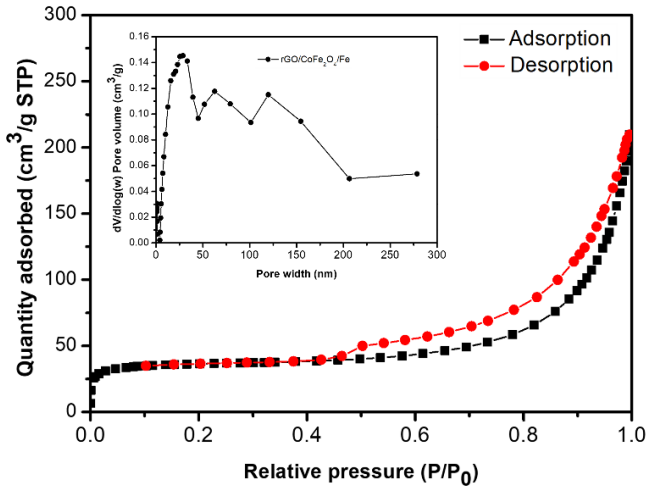

Figure 6. N_2 adsorption-desorption isotherms and the pore size distribution (inset) of rGO/$CoFe_2O_4$/Fe.

Figure 7(a) shows the UV-Vis adsorption spectrum of the rGO/$CoFe_2O_4$/Fe nanocomposite. The rGO/$CoFe_2O_4$/Fe gives a strong absorption in the range of 300 – 900 nm, indicating that rGO/$CoFe_2O_4$/Fe nanocomposite could be photocatalytically activated under visible light irradiation. Using this UV–Vis data, the band gap energy (E_g) of the rGO/$CoFe_2O_4$/Fe nanocomposite estimated using the Tauc equation [23] is 1.327 eV (Figure 7(b)), which is favorable for the photocatalytic process.

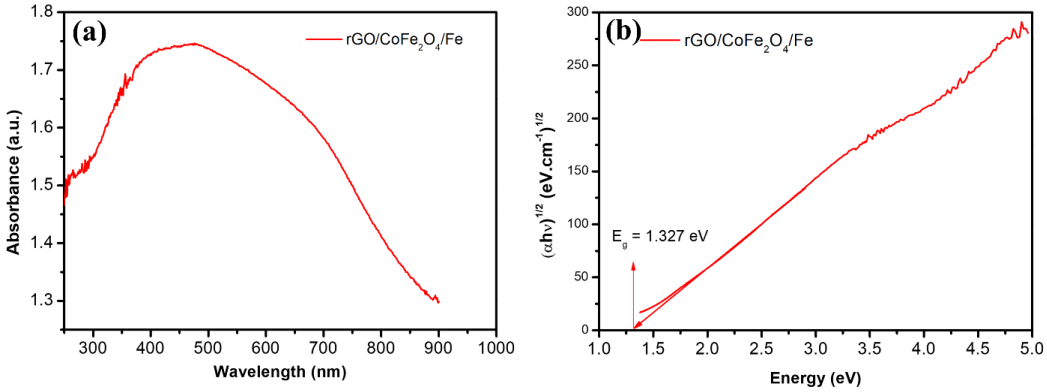

Figure 7. (a) UV-Vis DRS spectrum and (b) Tauc plot of as-synthesized rGO/$CoFe_2O_4$/Fe.

3.2. Photocatalytic performance of the synthesized materials

The removal of 4-NP in water was evaluated using different catalyst systems with reaction conditions of 10 mg4-NP/L, 150 mgcatalyst/L, 150 mgPMS/L, pH 7, and room temperature (~25 ^oC). As demonstrated in Figure 8(a), in the presence of PMS but without catalysts, the removal efficiency of 4-NP by chemical oxidation was only 14.70 %. In the presence of catalysts, the 4-NP removal efficiencies of rGO/$CoFe_2O_4$ and rGO/$CoFe_2O_4$/Fe by heterogeneous activation were 42.30 % and 68.69 %, respectively. Under visible light, the 4-NP photocatalytic removal efficiency increased to 76.47 % for rGO/$CoFe_2O_4$/PMS/Vis and 98.78% for rGO/$CoFe_2O_4$/Fe/PMS/Vis. In Figure 8(b) with the degradation of 4-NP over different catalytic systems, the correlation coefficient (R^2) values are very close to 1, consistent with the pseudo-first-order kinetic model. The k value of rGO/$CoFe_2O_4$/Fe/PMS/Vis is calculated to be 0.0361 min^{-1}, which is the highest among the prepared samples. Thus, rGO/$CoFe_2O_4$/Fe/PMS/Vis has a fast decomposition rate of 4-NP in water.

It is known that magnetic $CoFe_2O_4$ is used as a catalyst for PMS activation to degrade persistent organic substances in aqueous solution. The combination of iron and cobalt transition metals in the $CoFe_2O_4$ crystal structure is useful in increasing the $CoOH^+$ ions on the catalyst surface, which helps to further activate PMS (Reactions 1 - 3) [24]:

$$Fe^{3+} + H_2O \rightarrow FeOH^{2+} + H^+ \qquad (Re.\,1)$$

$$Co^{2+} + FeOH^{2+} \rightarrow CoOH^+ + Fe^{3+} \qquad (Re.\,2)$$

$$CoOH^+ + HSO_5^- \rightarrow CoO^+ + SO_4^{\bullet -} + H_2O \qquad (Re.\,3)$$

On the other hand, $CoFe_2O_4$ is active under visible light with narrow bandgap. After being excited by visible light, electrons (e^-) in valence band (VB) move to the conduction band (CB) of $CoFe_2O_4$, leaving holes (h^+) in the VB (Reaction 4). These e^- and h^+ can then react with PMS to form reactive oxygen species (ROSs) such as $SO_4^{\bullet -}$, $SO_5^{\bullet -}$, and $HO^{\bullet}$ (Reactions 5-9) [25] for the effective oxidation of 4-NP in water (Reaction 10).

$$CoFe_2O_4 + h\nu \rightarrow h^+ + e^- \quad \text{(Re. 4)}$$
$$HSO_5^- + e^- \rightarrow SO_4^{\bullet -} + OH^- \quad \text{(Re. 5)}$$
$$SO_4^{\bullet -} + OH^- \rightarrow SO_4^{2-} + HO^\bullet \quad \text{(Re. 6)}$$
$$SO_4^{2-} + h^+ \rightarrow SO_4^{\bullet -} \quad \text{(Re. 7)}$$
$$HSO_5^- + h^+ \rightarrow SO_5^{\bullet -} + H^+ \quad \text{(Re. 8)}$$
$$SO_5^{\bullet -} + SO_5^{\bullet -} \rightarrow 2SO_4^{\bullet -} + O_2 \quad \text{(Re. 9)}$$

$SO_4^{\bullet -}$, $SO_5^{\bullet -}$, and $HO^\bullet$ + 4-NP → intermediates + mineralized products (Re. 10)

Meanwhile, Fe^0 is used in this word instead of Fe^{2+} or Fe(II) in the conventional Fenton process. Besides the role as an additional source for the Fe^{2+} (Reactions 11-14), Fe^0 can react directly with PMS to produce $SO_4^{\bullet -}$ (Reaction 15) [26]:

$$Fe^{2+} + HSO_5^- \rightarrow Fe^{3+} + OH^- + SO_4^{\bullet -} \quad \text{(Re. 11)}$$
$$OH^- + SO_4^{\bullet -} \rightarrow HO^\bullet + SO_4^{2-} \quad \text{(Re. 12)}$$
$$Fe^0 \rightarrow Fe^{2+} + 2e^- \quad \text{(Re. 13)}$$
$$2Fe^{3+} + Fe^0 \rightarrow 3Fe^{2+} \quad \text{(Re. 14)}$$
$$Fe^0 + 2HSO_5^- \rightarrow Fe^{2+} + 2OH^- + 2SO_4^{\bullet -} \quad \text{(Re. 15)}$$

The combination of $CoFe_2O_4$ with Fe^0 NPs creates a novel hybrid material with many outstanding properties such as high photocatalytic and magnetic properties of $CoFe_2O_4$ and Fenton-like reaction of Fe^0. The results that the rGO/$CoFe_2O_4$/Fe/PMS/Vis system has high degradation efficiency and rate for 4-NP. Therefore, the rGO/$CoFe_2O_4$/Fe nanocomposite is very effective for removing 4-NP in water.

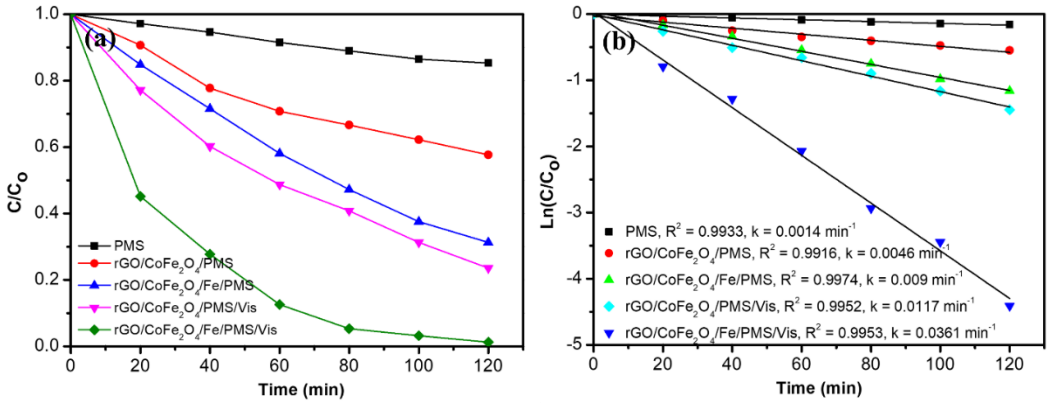

Figure 8. (a) 4-NP removal in different systems and (b) linear fitting of ln(C/C_0) versus t

(Conditions: [4-NP] = 10 mg/L, [Catalyst] = 150 mg/L, [PMS] = 150 mg/L, pH = 7, Temperature = 25 ^oC).

The UV-Vis molecular absorption spectrum of 4-NP over time using the rGO/$CoFe_2O_4$/Fe/PMS/Vis system is shown in Figure 9(a). The position of the maximum absorption wavelength of 320 nm for 4-NP is almost unchanged during the reaction time. However, its peak intensity gradually decreased over time, indicating the destruction of the 4-NP structure. This proves that under the effect of visible light, the rGO/$CoFe_2O_4$/Fe catalyst effectively activates PMS to form ROSs for 4-NP degradation.

The effect of the catalyst content is related to the number of surface active sites, PMS activation, and ROSs formation. As shown in Figure 9(b), the 4-NP removal efficiency increased with increasing catalyst dosage. Specifically, when catalyst content increased from 50 to 150

mg/L, the efficiency after 120 minutes increased from 44.16 % to 98.78 %, which would be explained as follows. By increasing the catalyst content, more active sites are created on the catalyst surface, which promotes PMS activation and causes a significant amount of ROSs to be produced for 4-NP degradation. However, when the catalyst concentration was increased to 250 mg/L, the efficiency marginally declined because too much catalyst makes the catalyst particles turbid, which inhibits light absorption and, in turn, reduces the amount of ROSs created. Additionally, exceeding the appropriate level of catalyst concentration can result in catalyst agglomeration, which slows down the rate of 4-NP breakdown by rendering a part of the catalyst surface incapable of absorbing photons. As a result, 150 mg/L was chosen as the ideal catalyst content for further studies.

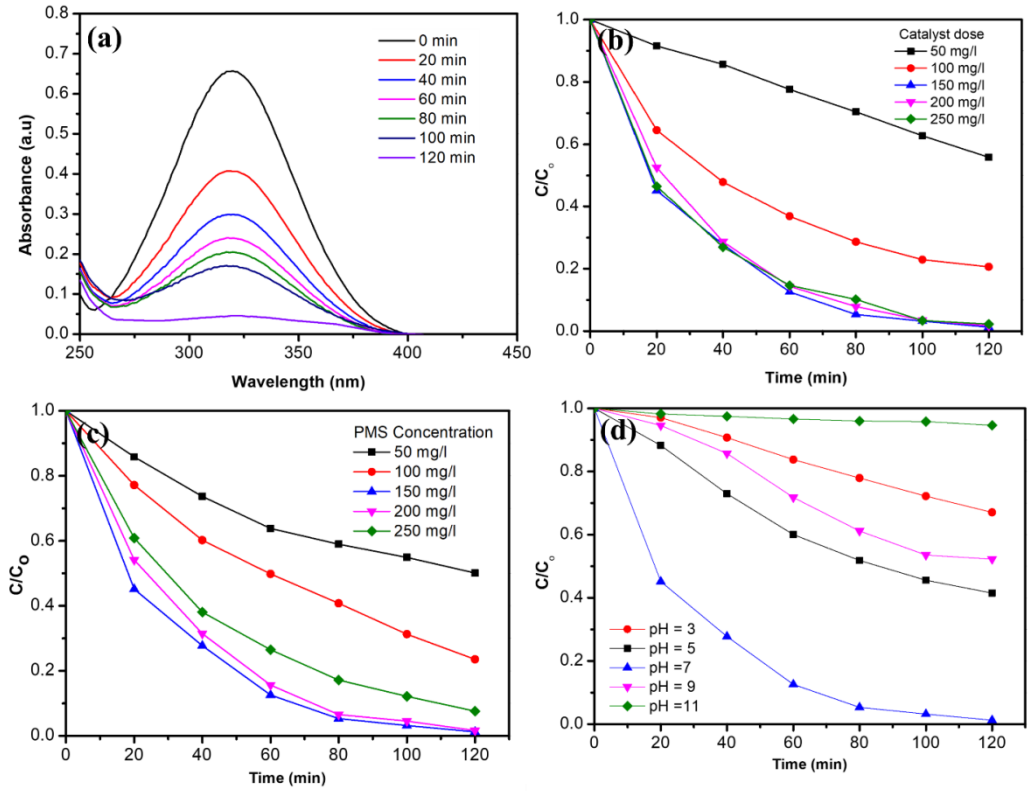

Figure 9. (a) Time-dependent UV-Vis spectra of rGO/$CoFe_2O_4$/Fe and effects of (b) catalyst dosage, (c) initial PMS concentration, and (d) pH

(Conditions: [4-NP] = 10 mg/L, [Catalyst] = 150 mg/L, [PMS] = 150 mg/L, pH = 7, Temperature = 25 ^oC).

Figure 9(c) demonstrates that when PMS concentration increased, the 4-NP removal efficiency increased dramatically. More specifically, after 120 minutes, the efficiency rose from 49.88 % to 98.78 % when the PMS concentration was increased from 50 to 150 mg/L. This may be because an increase in PMS concentration causes a significant quantity of generated ROSs, which accelerates the degradation of 4-NP. Additionally, PMS can facilitate electrons to depart the VB of rGO/$CoFe_2O_4$/Fe, which prevents electron and hole recombination while promoting photocatalytic processes [27]. The efficiency dropped to 92.38 % when the PMS content was increased to 250 mg/L. The formation of $SO_4^{\bullet-}$ which can react with itself or be broken down by too much PMS (Reactions 16-17) might be the cause. The high level of ROSs that is produced on the catalyst surface also contributes to the increased electron-hole recombination.

Additionally, a typical interaction between too much PMS and $SO_4^{\bullet-}$ can result in $SO_5^{\bullet-}$, which has a lower oxidation potential (E^o = 1.05 V) and slows down 4-NP degradation [28]. For the next studies, a PMS concentration of 150 mg/L was selected.

$$SO_4^{\bullet-} + SO_4^{\bullet-} \rightarrow S_2O_8^{2-} \quad \text{(Re. 16)}$$

$$SO_4^{\bullet-} + HSO_5^{-} \rightarrow SO_5^{\bullet-} + SO_4^{2-} + H^+ \quad \text{(Re. 17)}$$

Solution pH has a strong effect on the 4-NP degradation efficiency, as can be seen in Figure 9(d). In an acidic environment, H^+ and ─O─O─ bonds in PMS form hydrogen bonding, thus reducing the interaction probability between the PMS and catalyst surface. Furthermore, in an acidic environment, there is the decomposition of ROS into less active forms (Reactions 18-19) [29].

$$HO^{\bullet} + H^+ + e^- \rightarrow H_2O \quad \text{(Re. 18)}$$

$$SO_4^{\bullet-} + H^+ + e^- \rightarrow HSO_4^{\bullet-} \quad \text{(Re. 19)}$$

In an alkaline environment, the $SO_4^{\bullet-}$ converts to a weaker oxidizing $HO^{\bullet}$ (Reaction 20), resulting in a lower 4-NP degradation.

$$SO_4^{\bullet-} + HO^- \rightarrow SO_4^{2-} + HO^{\bullet} \quad \text{(Re. 19)}$$

The highest 4-NP degradation efficiency was 98.78% at pH 7. Since pH 7 is also a neutral and desired condition for safe operation.

4. CONCLUSIONS

rGO/$CoFe_2O_4$/Fe nanocomposite was successfully synthesized by a simple route. The spherical $CoFe_2O_4$ and Fe^0 NPs with diameters from 40 to 100 nm were well distributed on the surface of rGO sheets at high density. rGO/$CoFe_2O_4$/Fe has a good magnetic property (saturated magnetization of 31.8 emu/g at 11 kOe), fast degradation rate (k = 0.0361 min^{-1}), and high removal performance towards 4-NP (removal efficiency of 98.78% after 120 min under conditions of 10 mg4-NP/L, 150 mgcatalyst/L, 150 mgPMS/L, pH 7, and 25 ^oC). As a result, rGO/$CoFe_2O_4$/Fe promises a potential visible-light photo-Fenton-like magnetic catalyst for wide application in environmental remediation.

Acknowledgments There was no funding specific to this work.

CRediT authorship contribution statement Vu Dinh Thao: Ideas, Methodology, Experiment performing, Supervision, Funding acquisition, Draft manuscript. Nguyen Dinh Sinh, Nguyen Trung Dung, Vu Ngoc Toan: Conducting experiments, Formal analysis. Nguyen Nhat Huy: Revising manuscript, Critical review.

Declaration of competing interest. The authors declare that they have no known competing financial interests or personal relationships that could have appeared to influence the work reported in this paper.

REFERENCES

1. Shen J., Xu X., Jiang X., Hua C., Zhang L., Sun X., Li J., Mu, Y., Wang L. - Coupling of a bioelectrochemical system for p-nitrophenol removal in an upflow anaerobic sludge blanket reactor, Water Res. **67** (2014) 11-18.
2. Tummala S., Lee C. H., Ho Y. P. - Boron, and nitrogen co-doped carbon dots as a multiplexing probe for sensing of p-nitrophenol, Fe (III), and temperature, Nanotechnology **32** (2021) 265502.

3. Jin Z., Hu R., Wang Hu J., Ren T. - One-step impregnation method to prepare direct Z-scheme $LaCoO_3$/g-C_3N_4 heterojunction photocatalysts for phenol degradation under visible light, Appl. Surf. Sci. **491** (2019) 432-442.
4. Wang J., Wang S. - Activation of persulfate (PS) and peroxymonosulfate (PMS) and application for the degradation of emerging contaminants, Chem. Eng. J. **334** (2018) 1502- 1517.
5. Hassani A., Eghbali P., Kakavandi B. K.Y.A., Lin Ghanbari F. - Acetaminophen removal from aqueous solutions through peroxymonosulfate activation by $CoFe_2O_4$/mpg-C_3N_4 nanocomposite: Insight into the performance and degradation kinetics, Environ. Technol. Innov. **20** (2020) 101127.
6. L, Y.W., Ma W. L. - Photocatalytic oxidation technology for indoor air pollutants elimination: A review, Chemosphere **280** (2021) 130667.
7. Cao J., Lai L., Lai B., Yao G., Chen X., Song L. - Degradation of tetracycline by peroxymonosulfate activated with zero-valent iron: performance, intermediates, toxicity and mechanism, Chem. Eng. J. **364** (2019) 45-56.
8. Hu P., Long M. - Cobalt-catalyzed sulfate radical-based advanced oxidation: a review on heterogeneous catalysts and applications, Appl. Catal. B. **181** (2016) 103-117.
9. Duru I. P. - Electronic and magnetic properties of $CoFe_2O_4$ nanostructures: An ab-initio and Monte Carlo study, Physica B: Condensed Matter. **627** (2022) 413548.
10. Yao Y., Cai Y., Lu F., Wei F., Wang X., and Wang S. - Magnetic recoverable $MnFe_2O_4$ and $MnFe_2O_4$-graphene hybrid as heterogeneous catalysts of peroxymonosulfate activation for efficient degradation of aqueous organic pollutants, J. Hazard. Mater. **270** (2014) 61-70.
11. Long M. Y., Di Li., Li H. M., Ma X. G., Zhao Q. Q., Wen Q., Song F. - Synergetic effect of photocatalysis and peroxymonosulfate activated by MFe_2O_4 (M = Co, Mn, or Zn) for enhanced photocatalytic activity under visible light irradiation, RSC Adv.**12** (2022) 20946
12. Zhang K., Sun D., Ma C., Wang G., Dong X., Zhang X. - Activation of peroxymonosulfate by $CoFe_2O_4$ loaded on metal-organic framework for the degradation of organic dye, Chemosphere **241** (2020) 125021.
13. Du Y., Ma W., Liu P., Zou B., Ma J. - Magnetic $CoFe_2O_4$ nanoparticles supported on titanate nanotubes ($CoFe_2O_4$/TNTs) as a novel heterogeneous catalyst for peroxymonosulfate activation and degradation of organic pollutants, J. Hazard. Mater. **308** (2016) 58-66.
14. Pourzamani H., Jafari E., Rozveh M., Mohammadi H., Rostami M., Mengelizadeh N. - Degradation of ciprofloxacin in aqueous solution by activating the peroxymonosulfate using graphene based on $CoFe_2O_4$, Degradation of ciprofloxacin in aqueous solution by activating the peroxymonosulfate using graphene based on $CoFe_2O_4$, Desalin. water Treat. **167** (2019) 156-169.
15. Ng Y. H., Iwase A., Bell N. J., Kudo A., Amal R. - Semiconductor/reduced graphene oxide nanocomposites derived from photocatalytic reactions, Catal. Today **164** (2011) 353-357.
16. Li X., Yu J., Wageh S., Al-Ghamdi A. A., Xie J. - Graphene in photocatalysis: a review, Small **12** (2016) 6640-6696.
17. Ong W. J., Tan L. L., Chai S. P., Yong S. T., Mohamed A. R. - Surface charge modification via protonation of graphitic carbon nitride (g-C3N4) for electrostatic self-assembly construction of 2D/2D reduced graphene oxide (rGO)/g-C3N4 nanostructures

toward enhanced photocatalytic reduction of carbon dioxide to methane, Nano Energy **13** (2015) 757-770.

18. Thu T. V., Ko P. J, Phuc N. H. H., Sandhu A. - Room-temperature synthesis and enhanced catalytic performance of silver-reduced graphene oxide nanohybrids, J. Nanoparticle Res. **15** (2013) 1-13.
19. Yavari S., Mahmodi N. M., Teymouri P., Shahmoradi B., Maleki A. - Cobalt ferrite nanoparticles: preparation, characterization and anionic dye removal capability, J. Taiwan Inst. Chem. Eng. **59** (2016) 320-329.
20. Mazarji M., Esmaili H., Bidhendi G. N., Mahmoodi N. M., Minkina T., Sushkova S., Mandzhieva S., Barakhov A., Moghtaderi H., Bhatnagar A. - Green synthesis of reduced graphene oxide-$CoFe_2O_4$ nanocomposite as a highly efficient visible-light-driven catalyst in photocatalysis and photo Fenton-like reaction, Materials Science & Engineering B **270** (2021) 115223.
21. Su L. H., Liu C. W., Liang K. K., Chen Y. D., Zhang L. J., Li X. L., Han Z. H., Zhen G. Y., Chai X. L., and Sun X. - Performance evaluation of zero-valent iron nanoparticles (NZVI) for high-concentration H_2S removal from biogas at different temperatures, RSC.Adv. **8** (2018) 13798-13805.
22. Thu T. V., Thao V. D. - Influence of temperature on structure, morphology, and magnetic property of graphene–$MnFe_2O_4$ nanocomposites synthesized by a combined hydrothermal/co-precipitation method, Applied Physics A **124** (2018) 675
23. Makuła P., Pacia M., Macyk W. - How To Correctly Determine the Band Gap Energy of Modified Semiconductor Photocatalysts Based on UV–Vis Spectra, J. Phys. Chem. Lett. **9** (2018) 6814-681.
24. Rodríguez-Chueca J., Barahona-García E., Blanco-Gutiérrez V., Isidoro-García L., Dos santos-García A. J. - Magnetic $CoFe_2O_4$ ferrite for peroxymonosulfate activation for disinfection of wastewater, Chemical Engineering Journal **398** (2020) 125606.
25. Amini M. M., Mengelizadeh N. - Catalytic degradation of mefenamic acid by peroxymonosulfate activated with MWCNTs-$CoFe_2O_4$: influencing factors, degradation pathway, and comparison of activation processes, Environmental Science and Pollution Research. https://doi.org/10.1007/s11356-020-10427-6, 2020.
26. Fu X. Y., Zhang J., Zhao H. D., Zhang S. J., Nie T., Zhang Y. T., Lu J. F. - Enhanced peroxymonosulfate activation by coupling zeolite-supported nano-zero-valent iron with weak magnetic field, Separation and Purification Technology **230** (2020) 115886.
27. Guo S., Yang Z., Zhang H., Yang W., Li J., Zhou K. - Enhanced photocatalytic degradation of organic contaminants over CaFe2O4 under visible LED light irradiation mediated by peroxymonosulfate, Journal of Materials Science & Technology **62** (2021) 34-43
28. Alnaggar G., Hezam A., Drmosh Q., Ananda S. - Sunlight-driven activation of peroxymonosulfate by microwave synthesized ternary $MoO_3/Bi_2O_3/g\text{-}C_3N_4$ heterostructures for boosting tetracycline hydrochloride degradation, Chemosphere **272** (2021) 129807.
29. Yang X. H., Fu H. T., An X. Z., Jiang X. C., Yu A. B. - Synthesis of $V_2O_5@TiO_2$ core-shell hybrid composites for sunlight degradation of methylene blue, RSC Adv. **6** (2013) 34103-34109.